sensors

MDPI

Article

Dynamic modeling of weld bead geometry features in thick plate GMAW manufacturing with typical joints based on machine vision and learning

Yinshui He[1], Daize Li[1], Zengxi Pan[2], Guohong Ma[3], Lesheng Yu[3], Haitao Yuan[3] and Jian Le[4]*

[1] School of Resources Environmental & Chemical Engineering, Nanchang University, Nanchang, 330031, China

[2] School of Mechanical, Materials, Mechatronic and Biomedical Engineering University of Wollongong, Wollongong, NSW, Australia

[3] Key Laboratory of Lightweight and High Strength Structural Materials of Jiangxi Province, Nanchang, 330031, China

[4] School of Information Engineering, Nanchang University, Nanchang, 330031, China (***Corresponding author**)

Abstract Weld bead geometry features (WBGFs) such as the bead width, height, area and center of gravity, are the common factors for weighing welding quality control. Effective modeling of these WBGFs contributes to implementing timely decision making of welding process parameters to improve welding quality and efficiency and enhance automatic levels. In this work, a dynamic modeling method of WBGFs is presented based on machine vision and learning in multipass gas metal arc welding (GMAW) with typical joints. A laser vision sensing system is used to detect weld seam profiles (WSPs) during the GMAW process, and a novel WSP extraction method is proposed with scale-invariant feature transform and machine learning. The feature points of the extracted WSP, namely the boundary points of the weld bead, are identified with slope mutation detection and number supervision. In order to stabilize the modeling process, a fault detection and diagnosis method is implemented using cubic exponential smoothing, and the diagnostic accuracy is within 1.50 pixels. Before modeling of WBGFs, a linear interpolation method is presented to implement sub pixel discrimination of the weld bead. With the effective feature points and the extracted WSP, a scheme of modeling the area, the all-position bead width and height and the center of gravity of the weld bead is presented. Experimental results show that the proposed method in this work adapts to the variable features of the weld bead in thick plate GMAW with T-joints/butt, and is also applicable for lap joints. This work can provide more evidences to control weld formation during thick plate GMAW manufacturing by optimizing welding process parameters in real time.

Keywords: Weld bead geometry features; visual all-position measurement; thick plate gas metal arc welding; machine vision and learning; fault detection and diagnosis

1. Introduction

The gas metal arc welding (GMAW) process has become a popular method for joining the thick plates of steel structures and is the most common joining method used in the shipbuilding industry, marine engineering equipment and pipe manufacturing [1, 2] etc. Automatic and intelligent welding technologies have been widely applied to the thick plate GMAW process, such as automatic seam tracking [3] and weld formation monitoring, to enhance welding quality and efficiency [4]. During thick plate GMAW, online control of weld formation for each pass is necessary and an essential prerequisite for weldment quality control, and welding process parameters are deemed the main factors that exceedingly influence weld formation [5-7]. Weld bead geometry features (WBGFs) can reflect welding process parameters and provide effective evidences to suggest how to optimize

welding process parameters because the relationship can be built with various models [8-10]. Thus, the real-time modeling of WBGFs is the really-demanded technology for the effective control of weld formation especially during the arc welding process.

The modeling process of WBGFs is implemented in an offline and online fashion. In some studies, prediction or optimization of WBGFs is the main objective using regression models between WBGFs and welding process parameters. In this case offline modeling methods are usually presented with the metallurgical microscope [11], the caliper [12], the optical microscope [13, 14] and the Machinist's microscope [15] in lap joint GMAW. All these studies where the measurement process is conducted with human intervention, are dependent on the visual ability of the evaluator [16]. For the offline modeling process, a better option is the non-contact type measurement methods such as ultrasonic sensing [17] and infrared sensors to control the depth of penetration and the bead width [18] etc.

The vision sensing technology is one of the main online measurement methods of WBGFs and the most common method for welding position detection [19, 20]. This kind of technology usually uses active or passive sensors to detect targets, and image processing methods are responsible for the extraction of WBGFs. During the measurement process with passive vision systems, multiple cameras are used to respectively detect the bead width and height [21], or a single high-speed camera is used combing with the image calibration technology [22]. For the active vision system, researchers generally use the laser to illuminate the weld bead to create a deformation proportional to the bead width and height. WBGFs are hence modeled by detecting the bead edges such as using Canny edge detection [23, 24].

With the development of machine vision and learning, laser vision sensing has been used in the welding industry because it can detect deep grooves with thick steel plates and simultaneously measure multiple WBGFs. In these studies, the sensor emits a laser light with the specific wavelength onto the groove, and a CCD camera captures the image. If the sensor works statically, the 2D measurement of WBGFs can be realized [25], and 3D WBGF measurement can be implemented by using a gantry or a robot to move the sensor along the welding direction [26-28] using image processing technologies.

It is noteworthy that the current studies mainly concentrate on the modeling of WBGFs for single weld bead during different welding processes, most of them are implemented for lap joints, and WBGFs usually are the bead width and height. More WBGFs such as the area and the center of gravity are also useful for weld formation control. In addition, the real-time modeling process of these WBGFs in thick plate GMAW with typical joints is full of more difficulties such as higher adaptability of information acquisition, variable WBGFs and stable determination of the weld bead involving two welding processes. These characteristics demand more effective WSP extraction and feature point identification methods, stable seam tracking technologies and the effective modeling scheme of the WBGFs. Also, the measurement of WBGFs at different formation positions at the same sampling time provides more direct evidences to optimize the welding process parameters (e.g. the angle of the welding torch) than the one in which WBGFs are counted up only at different sampling time.

Various WSP extraction methods have been reported in the literature [29, 30]. However, the extraction process of WSPs with larger sizes during the multipass welding process faces a bigger challenge. One of the reasons is that the extraction process with larger WSPs is easily disturbed. It is no doubt that an appropriate fault detection and diagnosis process [30] contributes on higher accuracy of visual feature acquisition and stability. The cubic exponential smoothing algorithm can predict future states of the research object using the past sampling for time series variables, and it has been applied to different industries [31, 32] for the optimization or prediction purpose.

This work uses a laser vision sensor to detect the deep groove with T-joints and butt joints during the multipass GMAW process and presents a more effective WSP extraction method based on scale-invariant feature transform (SIFT) and machine learning algorithms to strengthen the robustness comparing with the previous ones [33, 34]. This extraction method adapts to variable

WSPs. The feature points of the extracted WSP are effectively identified through slope mutation detection and supervising the number. In order to stabilize the seam tracking process and the subsequent modeling process of WBGFs, a fault detection and diagnosis process via the cubic exponential smoothing method is applied to the feature point identification process. A scheme of the modeling of WBGFs is proposed using the diagnosed feature points. With the proposed method in this work, the area, the center of gravity and the all-position bead width and height of the variable weld bead are modeled in real time for different passes. The effectiveness of the proposed method is validated by modeling the related WBGFs in lap-joint GMAW. The proposed method here contributes to implementing timely decision making of welding process parameters to improve welding quality and enhance automatic levels.

This work consists of WSP extraction, feature point identification of the WSP, fault detection and diagnosis, modeling of WBGFs, experimental results and conclusions.

2. WSP extraction with SIFT and machine learning

In order to monitor the WBGFs, especially the center of gravity of the weld bead, simultaneous imaging of the welding torch and the WSP is investigated through special combination of dimmer glass and the filter (**Fig. 1**). Experiments show that when the central wavelength of the filter is about 660 nm and the half bandwidth is 20 nm, and the transmittance of the dimmer glass is about 0.02%, the welding torch can be marked with the welding wire. The direction detection of the welding torch contributes to weld formation control. Here only the WSP extraction process is given as follows, and WSP extraction with T-joints is used as an example.

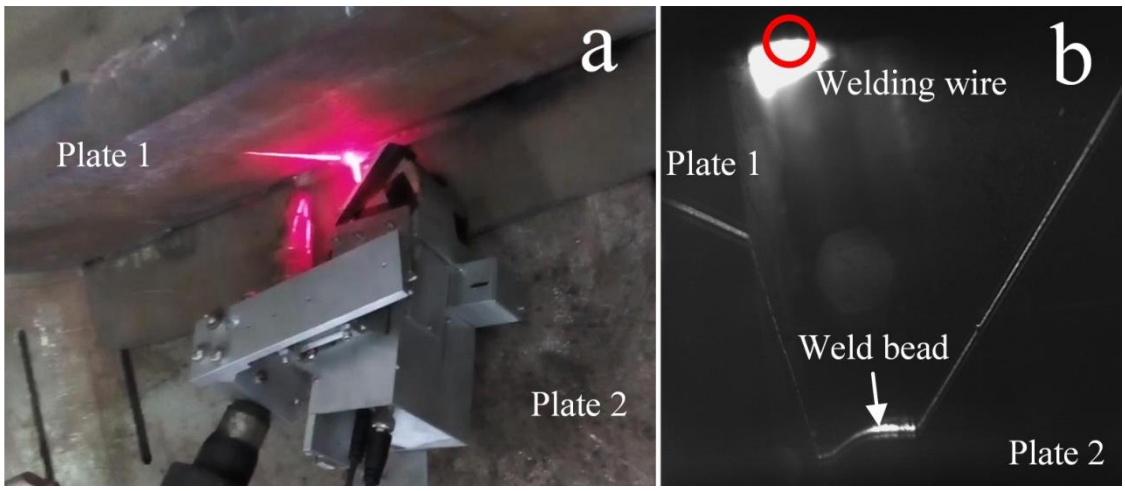


Figure 1. a Laser vision sensor. **b** The typical image captured during the multipass welding process.

One of the characteristics is the variable WSPs during the multipass GMAW process with typical joints. During the welding process, the welding torch with the laser vision sensor first moves to the welding position, and the latter works to detect the welding position for automatic seam tracking. After the welding position is determined, the real welding process begins. Two facts are that the image without arc is captured ahead of the move of the welding torch, and this image has the similar laser stripe (the shape, the position and the intensity) with the one captured during the welding process. The WSP extraction method is thus proposed based on SIFT and machine learning shown in **Fig. 2**.

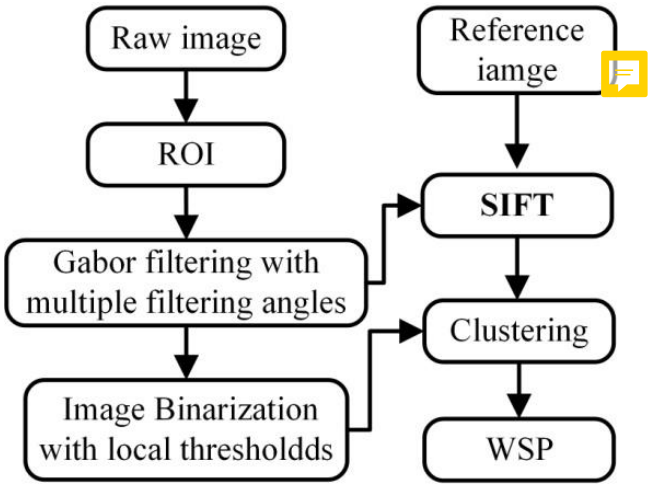


Figure 2. Flow chart of the WSP extraction method proposed in this work.

In this method, raw image means the image captured during the welding process while reference image is the one captured before arcing. The method includes two image processing paths. The first one is using the Gabor filter and local thresholds to highlight the WSP from background and simplify the background data, respectively. The second one is locating the WSP from the interference data based on clustering results using the nearest neighbor algorithm.

Region of interest (ROI) is normally used to reduce the influence of the interference data on WSP extraction and the computational burden [35]. There is a complete arc region in the image (**Fig. 3a**), and it has the maximum intensity. The global binarization is conducted with the maximum intensity (**Fig. 3b**), and the region below the bottom boundary of the arc region is the ROI in this work (**Fig. 3c**).

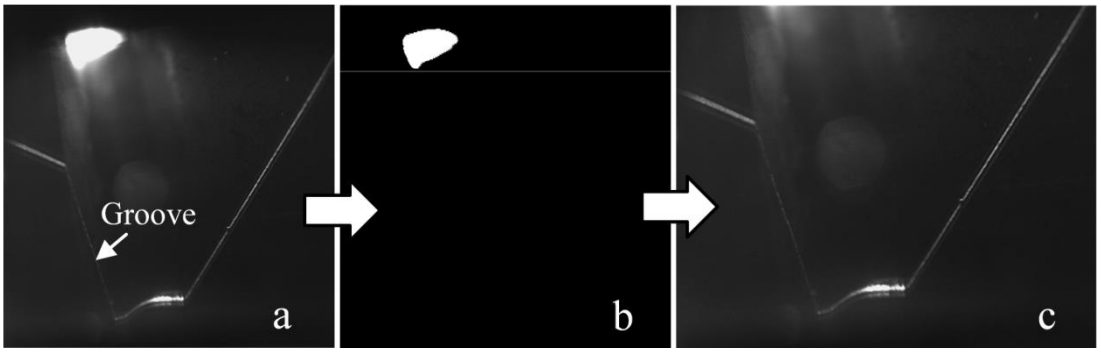


Figure 3. ROI determination process. **a** Raw image. **b** Binarization result to determine the ROI. **c** ROI.

2.1. Gabor Filtering

Gabor filtering is a classic orientation feature detection method mostly used in image or video processing [29]. The orientation features of the WSP are salient and most of them do not change much except the part of the weld bead during the multipass welding process. A great number of tests show that three specific filtering angles -12°, 15° and 90° can effectively highlight the WSP from the arc background as

$$F_o = 0.2G_{-12^{\circ}} + 0.3G_{15^{\circ}} + 0.5G_{90^{\circ}} \quad (1)$$

where F_o is the computational orientation feature map and G represents the Gabor filtering result [29]. The weight 0.5 accounts for the relatively low intensity of the groove region.

2.2. Local Thresholding

The local thresholds are determined as

$$T_i = \max_j [F_o(j-2:j+2, i-2:i+2)] \quad (2)$$

where i and j represent the row and column of the image respectively and T_i is the ith local threshold used for the region ranging from ith-2 to ith+2 columns when the columns are limited from j-2 to j+2.

2.3. WSP Location Using SIFT

SIFT is a method for extracting distinctive invariant features from two target images. It can be used to perform reliable matching between different views of an object or scene. These features are invariant to image scale and rotation [36]. These characteristics make SIFT can be used to locate the WSP through detecting their common features. In this work, reference image and the captured image are the input images, and these features are shown with a certain amount of matching points. The ratio of vector angles from the nearest to the second nearest neighbor highly influences the number of the matching points that are used to locate the WSP. Tests show the number increases with the ratio that is set from 0.9 to 0.99 (**Fig. 4**). However, the higher the ratio, the more are fake matching points. The ratio is set to 0.95 in this work.

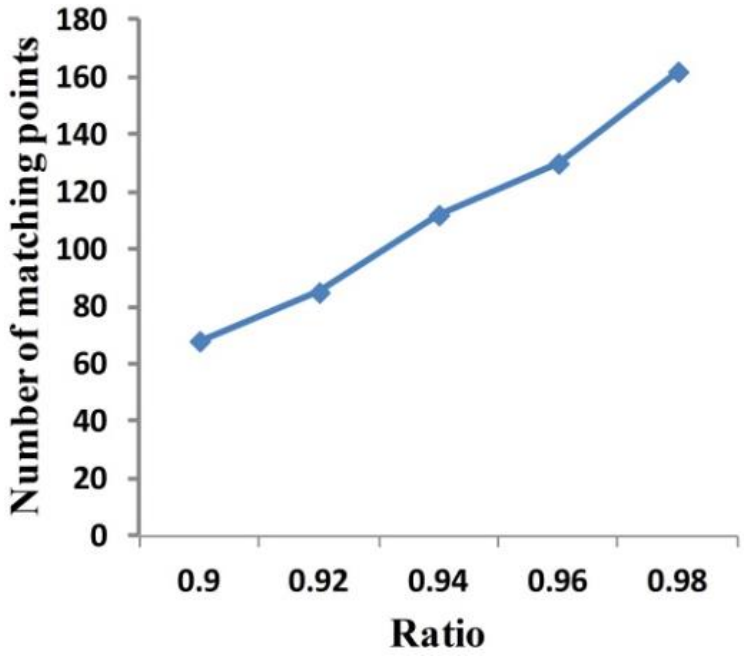


Figure 4. The relationship between the ratio and the number of matching points.

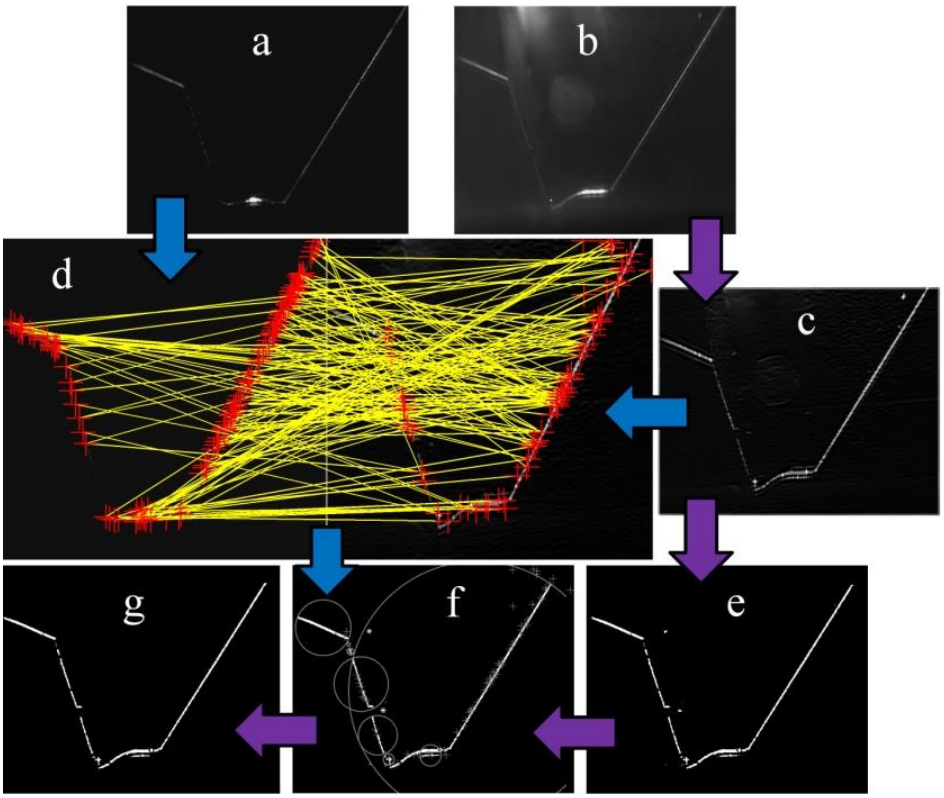


Figure 5. WSP extraction process based on SIFT and orientation feature detection. **a** Reference image. **b** ROI. **c** Orientation feature map. **d** Feature matching result using SIFT (red "+" represents the matching points). **e** Bizarization result using local thresholds. **f** Clustering result. **g** WSP extraction result.

In the other processing path, orientation feature map is binarized via local thresholds, and is followed with the nearest neighbor clustering that is used to mark the segments of the WSP. The cluster that is the nearest to the matching points is considered as a part of the WSP. The WSP extraction process is demonstrated in **Fig. 5**. The two kinds of arrows represent two processing paths. The method proposed here adapts to variable WSPs with higher robustness. It is a valuable reference to visual information acquisition in which visual-sensing-based technologies are used in the automatic welding process.

3. Feature Point Identification

The feature points in this work mean the boundary points of the weld bead and the groove. They are identified with least squares fitting [33], Hough transform [35], search algorithm [37] and slope detection [38] etc. The challenges of identifying all feature points are the variable WSPs and the unknown number of the feature points during the multipass GMAW process. In order to overcome these adverse factors and possible imperfect WSP extraction results (some interference data points are kept), this work presents an effective feature point identification method shown in **Fig. 6**.

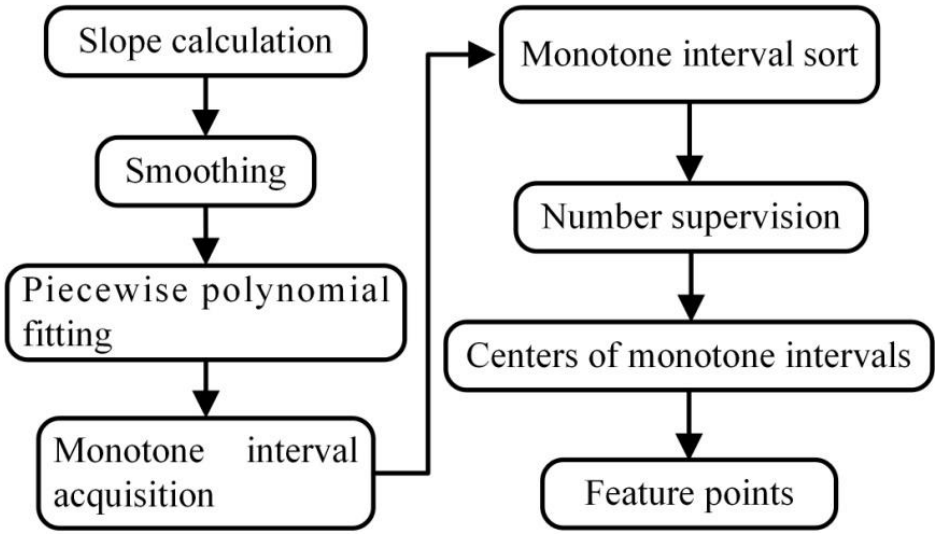


Figure 6. Flow chart of identifying the feature points of the extracted WSP.

Due to the discrete data points of the extracted WSP, the slopes of the extracted WSP easily fluctuate with the remaining interference data points and the distorted data points after the extracted WSP has been thinned (the average in the vertical direction) and interpolated with the least square method. The slope calculation process is based on smoothing processing as

$$k_i = \frac{1}{n}\sum_{j=1}^{n}\frac{y_i - y_j}{x_i - x_j} \qquad (3)$$

where n is the number of the involved data points for calculating the ith slope, and k is the slope vector. k still fluctuates abnormally. Without loss of generality, a one-dimensional linear filter is used to smooth k with the size 1×9. Piecewise polynomial fitting is used to further approach the actual variation characteristics of k respectively using a half data points of k as

$$K_i = \sum_{j=0}^{30} a_j^i (k_{h_i})^j (i = 1, 2) \qquad (4)$$

where $K_i(i=1,2)$ is the fitting slope vector, $a_j^i(i=1,2)$ are two sets of coefficients, and k_{h_i} is each half of k. Monotone interval acquisition is implemented with (5):

$$\begin{cases} k(i-1) \geq k(i) \geq k(i+1) \\ k(i-1) \leq k(i) \leq k(i+1) \end{cases} \qquad (5)$$

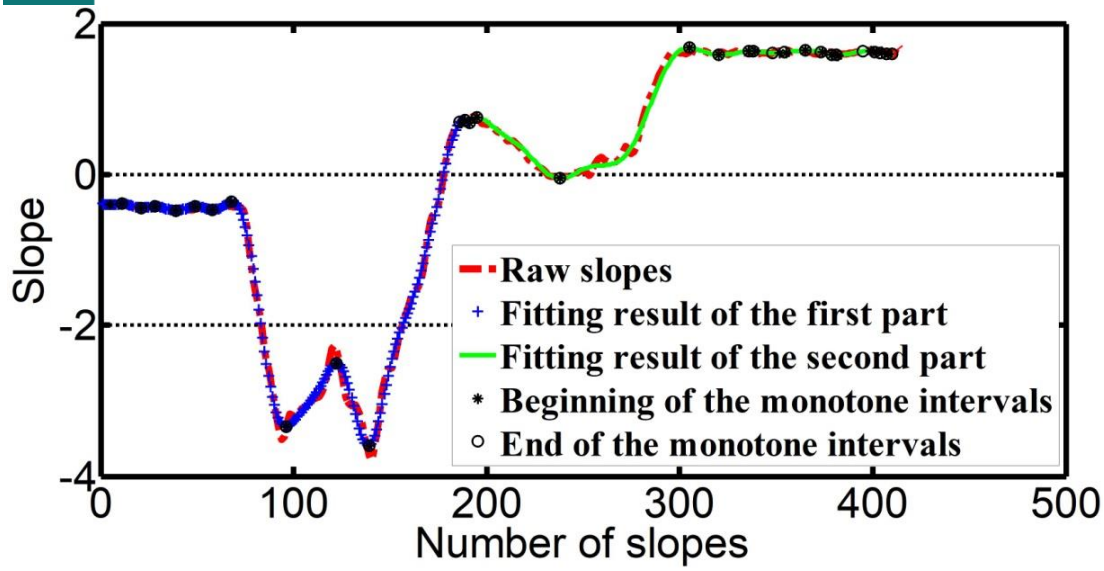


Figure 7. Slope piecewise fitting and monotone interval acquisition.

$MI = \{mi_i\}, i = 1, 2, \cdots N$ represents the monotone intervals, and $\{mi_i^b\}$ and $\{mi_i^e\}$ are respectively the start and the end slopes of MI (**Fig. 7**). The length of the monotone interval is defined as $l_{MI} = \left|\{mi_i^b\} - \{mi_i^e\}\right|$. The lengths of MI are sorted in ascending order. After the supervision number (e.g. P) of the feature points is determined, the first P monotone intervals of MI' are selected. The serial number of each selected monotone interval indicates the position of the feature points in the vector MI.

The effectiveness of the feature point identification method proposed here is validated with the images captured during the welding process shown in **Fig. 8**. The experimental results show that 95.6% of the images can be identified precisely with the error of 3 pixels, and the feature points deviate from the actual positions when there is some interference such as splash, welding slag, etc., near these positions (**Fig. 9**). That needs the error correction mechanism to predict/optimize the feature point when it is considered as the tracking point. Multithreading processing is used to predict/optimize multiple feature points that are utilized to implement the measurement of WBGFs.

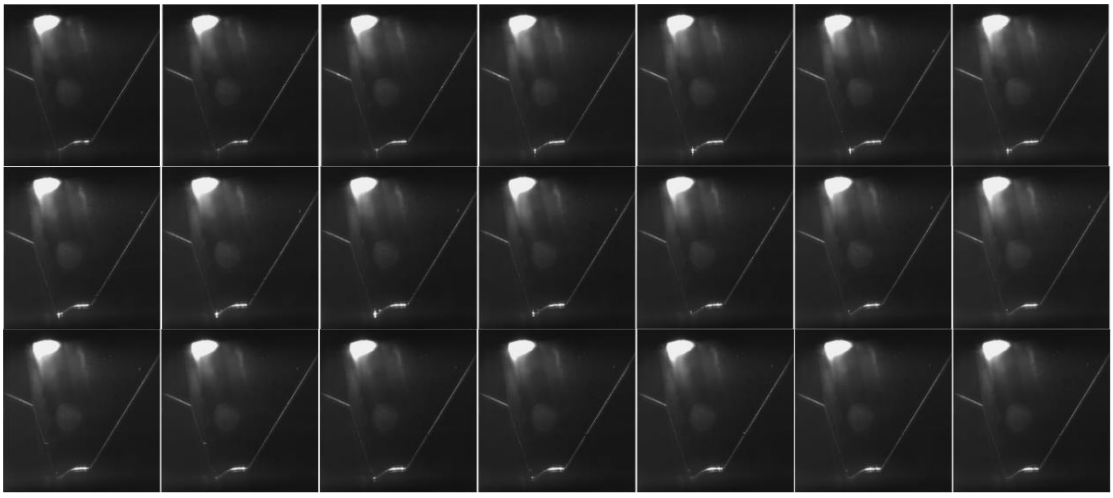


Figure 8. Images captured during the welding process for feature point identification test.

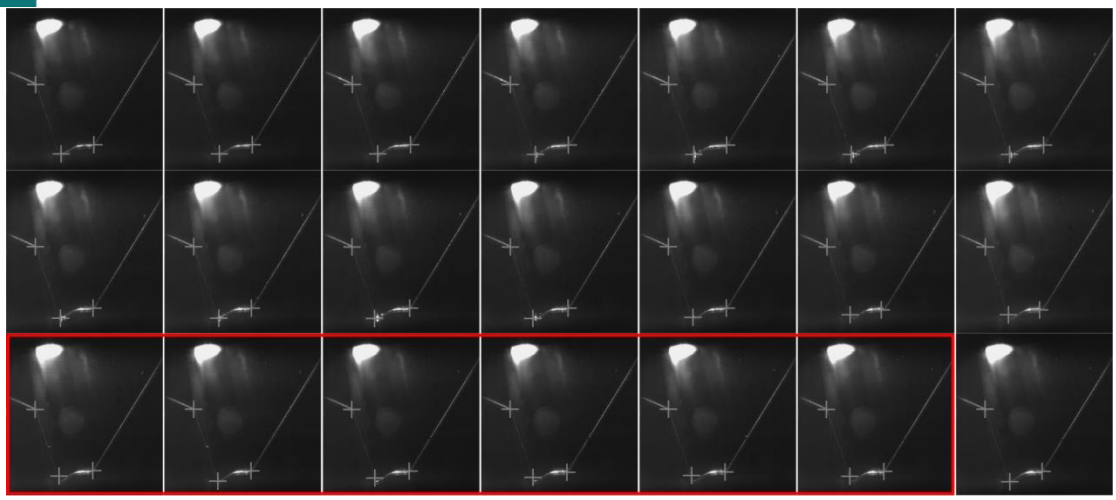


Figure 9. Feature point identification results in which the images in the red rectangle show the examples of ineffective feature identification.

4. Cubic Exponential Smoothing for Stabilizing Feature Point Identification Process

The cubic exponential smoothing method is typically used to stabilize time serial variables through predicting the real states for several sampling periods in the future. The method is effective when the time serial variable fluctuates periodically and/or in a linear trend. Once the workpiece is fixed, the deviations of all feature points between the start and the end welding points are constants in all directions except the welding direction. These feature points occur in a linear trend. They can thus be predicted with the cubic exponential smoothing method when the ineffective feature point identification result is diagnosed. The state of the target feature point is iterated over as

$$\begin{cases} S_t^{(1)} = \alpha x_t + (1-\alpha) S_{t-1}^{(1)} \\ S_t^{(2)} = \alpha S_t^{(1)} + (1-\alpha) S_{t-1}^{(2)} \\ S_t^{(3)} = \alpha S_t^{(2)} + (1-\alpha) S_{t-1}^{(3)} \end{cases} \quad (6)$$

where α is the smoothing coefficient, and x_t is the coordinates of the target feature point in the y-/x-direction in images (suppose that they are independent). The coordinates of the target feature point is predicted/optimized as

$$x_{t+T} = A_t + B_t T + C_t T^2 \quad (7)$$

where T is the sampling period, and the coefficients A, B and C are computed as

$$\begin{cases} A_t = 3S_t^{(1)} - 3S_t^{(2)} + S_t^{(3)} \\ B_t = \dfrac{\alpha}{2(1-\alpha)^2}[(6-5\alpha)S_t^{(1)} - 2(5-4\alpha)S_t^{(2)} + (4-3\alpha)S_t^{(3)}] \\ C_t = \dfrac{\alpha^2}{21(1-\alpha)^2}[S_t^{(1)} - 2S_t^{(2)} + S_t^{(3)}] \end{cases} \quad (8)$$

where x_t is initialized with the coordinate of the corresponding feature point of the reference image (see Section 2)

The triggers of stating the smoothing process using the cubic exponential smoothing method is the abnormal distance between the last effective result and the current identification result that is nearest to the target feature point. The cubic exponential smoothing algorithm works when the abnormal distance is bigger 3 pixels. The prediction process is the one-step prediction method. The typical process is given in ***Algorithm 1***.

Algorithm 1: Algorithm of predicting/optimizing the feature point using cubic exponential smoothing

Input: x_t, α

Output: x_{t+1}

- Feature point ineffectiveness judgment: $\left\| x'_{t+1} - x_t \right\| \geq 3$ *pixels*

* $S_t^{(1)} = \alpha x_t + (1-\alpha) S_{t-1}^{(1)}$

$S_t^{(2)} = \alpha S_t^{(1)} + (1-\alpha) S_{t-1}^{(2)}$

$S_t^{(3)} = \alpha S_t^{(2)} + (1-\alpha) S_{t-1}^{(3)}$

* Calculate A_t, B_t and C_t

$$A_t = 3S_t^{(1)} - 3S_t^{(2)} + S_t^{(3)}$$

$$B_t = \frac{\alpha}{2(1-\alpha)^2}[(6-5\alpha)S_t^{(1)} - 2(5-4\alpha)S_t^{(2)} + (4-3\alpha)S_t^{(3)}]$$

$$C_t = \frac{\alpha^2}{21(1-\alpha)^2}[S_t^{(1)} - 2S_t^{(2)} + S_t^{(3)}]$$

* Calculate x_{t+1}

$$x_{t+1} = A_t + B_t + C_t$$

- x'_{t+1} is replaced with x_{t+1}

x'_{t+1} is the coordinate of the current identified feature point.

The images within the red rectangle in **Fig. 9** are optimized with the cubic exponential smoothing method shown in **Fig. 10** and the optimized data in the horizontal/vertical direction is given in **Fig. 11**. Through this diagnostic process, the accuracy of identifying the feature points is within 1.50 pixels overcoming any random interference.

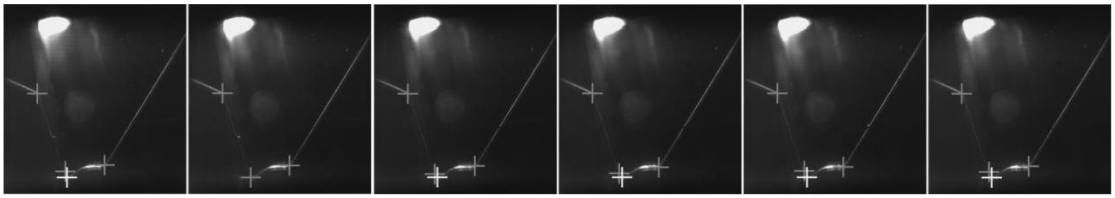


Figure 10. Optimization results of ineffective feature point identification using the cubic exponential smoothing method (white "+" indicates the optimized feature points).

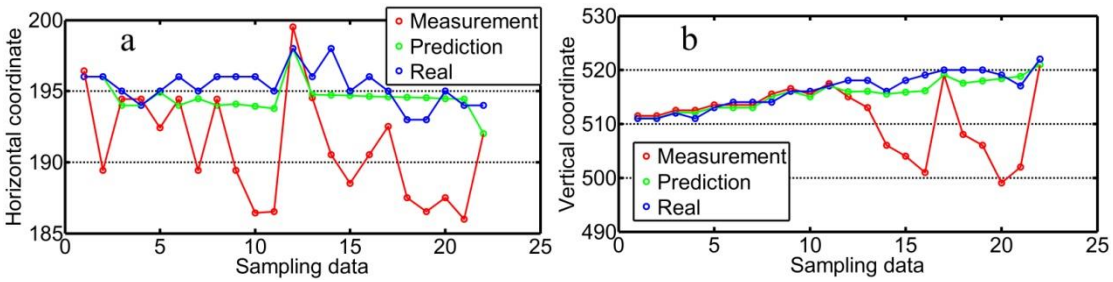


Figure 11. Prediction function display of the cubic exponential smoothing method. **a** Prediction result of the horizontal coordinate of the target feature point with an accuracy of 1.56 pixels. **b** Prediction result of the vertical coordinate of the target feature point with an accuracy of 1.43 pixels.

Experimental results show that the cubic exponential smoothing method enhances the accuracy of feature point identification and can be used to restrain the abnormal fluctuation of the tracking

target in the visual-sensing-based information acquisition process. This process stabilizes seam tracking and the subsequent measurements of WBGFs.

5. Modeling of WBGFs

5.1. Sub Pixel Discrimination of WBGFs

In order to improve modeling accuracy, linear interpolation is applied to sub pixel discrimination of the weld bead before modeling as

$$O_i^{'} = \frac{A_{i+1} - A_i^{'}}{A_{i+1} - A_i} O_i + \frac{A_i^{'} - A_j}{A_{i+1} - A_i} O_{i+1} \qquad (9)$$

where O_i, A_i, O_{i+1} and A_{i+1} are the coordinates of two adjacent pixels in the region of the weld bead in images, and $A_i^{'}$ and $O_i^{'}$ are the coordinates of interpolation points. Between two adjacent pixels, nine points are linearly interpolated.

5.2. Modeling Process of WBGFs

The WBGFs of the weld bead include the area, the center of gravity and the all-position bead width and height in this work. The modeling scheme is illustrated in **Fig. 12**.

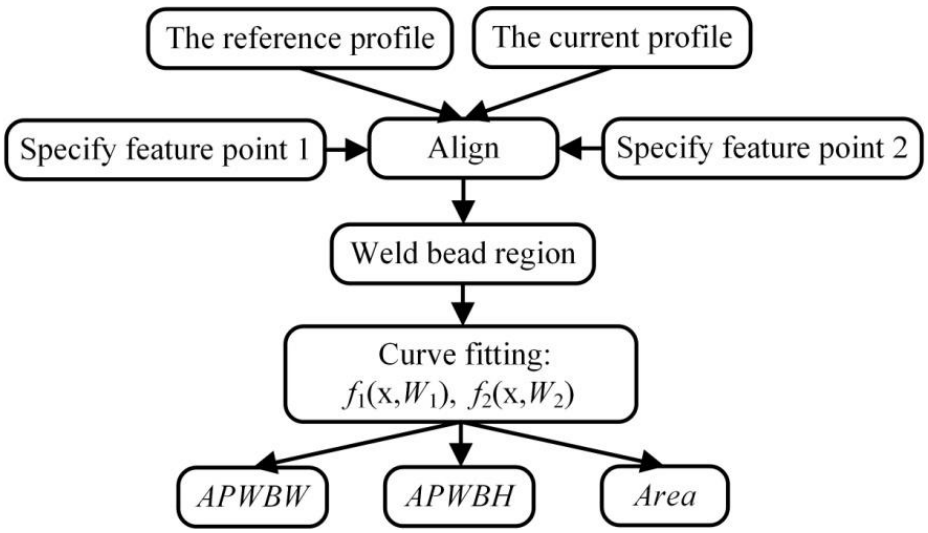


Figure 12. Scheme of WBGF modeling.

The reference profile is from the reference image. The two profiles are aligned by overlapping a common feature point (e.g. the leftmost feature point in T-joint and butt joint welding). The bead region is determined after some feature points of two input WSPs are designated respectively. The region consists of the lower and upper curve lines. That is, the upper boundary is first determined with the corresponding feature points, the start point of the lower boundary is then the nearest point to the left of the upper boundary, and the end point of the lower boundary is also the nearest point to the right of the upper boundary. There are two gaps between the two boundaries. Two lines are defined with two-point form of straight-line equations (**Fig. 13**) to connect the two boundaries:

$$y^i = \frac{y_{1i} - y_{2i}}{x_{1i} - x_{2i}}(x - x_{1i}) + y_{1i} \quad (i = 1, 2) \qquad (10)$$

where x_{1i}, y_{1i}, x_{2i} and y_{2i} $(i=1,2)$ are the coordinates of the two sets of the endpoints of the curve lines in images. The gaps are filled using the two straight-line equations. The weld bead in images is thus a closed region.



Figure 13. Example of filling the gaps between two boundaries of the weld bead in images (the grey data points that are marked with two blue circles are the filled data points).

The data points respectively belonging to the upper and lower boundaries are $\{Dt_i^1\}(i=1,2,\cdots Q)$ and $\{Dt_i^2\}(i=1,2,\cdots M)$. Polynomial fitting is used to model the boundaries of the weld bead as

$$\begin{cases} f_1(Dt_i^1, W_1) = \sum_{j=0}^{N} \omega_j (Dt_i^1)^j \\ f_2(Dt_i^2, W_2) = \sum_{j=0}^{N} \omega_j^{'} (Dt_i^2)^j \end{cases} \quad (11)$$

where N is the order and initialized to 10. In order to implement the all-position measurement process, two ranges of the weld bead in images are first determined as $\{LR_j\}(\{LR_j\} = \{f_1(Dt_i^1, W_1)\}_x \cap \{f_2(Dt_i^2, W_2)\}_x)$ in the vertical direction and $\{UD_j\}(\{UD_j\} = \{f_1(Dt_i^1, W_1)\}_y \cup \{f_2(Dt_i^2, W_2)\}_y)$ in the horizontal direction. For $\forall a_j \in [\min(\{LR_j\}), \max(\{LR_j\}))]$, there exist two points and the line $x = a_j$ such that the distances respectively between the two points and the line $x = a_j$ are both one pixel. The two points are actually the two intersection points of the closed weld bead region and the vertical line $x = a_j$. Their ordinates are A_{j1} and A_{j2}, respectively. Also, for $\forall b_j \in [\min(\{UD_j\}), \max(\{UD_j\}))]$, there exist another two points and the line $y = b_j$ such that the distances respectively between the two points and the line $y = b_j$ are both one pixel. The abscissas of the two points are O_{j1} and O_{j2} (**Fig. 14**). The all-position weld bead width (*APWBW*) is then measured with **12**, the all-position weld bead height (*APWBH*) is calculated with **13**, and the area measurement of the weld bead is implemented with **14**.

$$APWBW = |O_{j1} - O_{j2}| \quad (12)$$

$$APWBH = |A_{j1} - A_{j2}| \quad (13)$$

$$Area = (\int [f_1(Dt_i^1, W_1) - f_2(Dt_i^2, W_2)]dx \Big|_{\min(\{LR_j\})}^{\max(\{LR_j\})} \quad (14)$$

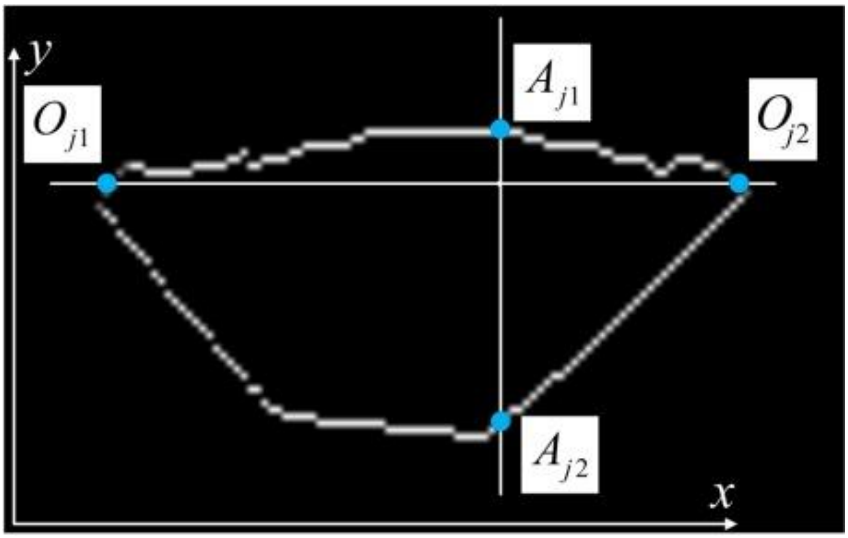


Figure 14. Diagrammatic sketch of determining the *APWBW* and the *APWBH*.

In addition, we think that the center of gravity of the weld bead is also a useful feature, which can guide the effective adjustment of the angle of the welding torch. The zero and first moment of the binary image is used to compute the coordinate of the center of gravity as

$$\begin{cases} x_c = \sum_i \sum_j j \cdot v(i,j) / \sum_i \sum_j v(i,j) \\ y_c = \sum_i \sum_j i \cdot v(i,j) / \sum_i \sum_j v(i,j) \end{cases} \quad (15)$$

where $v(i,j)$ is the gray value at point (i,j), and x_c, y_c are the corresponding coordinates of the center of graviy in two directions. It is marked with "+" in images.

6. Experimental Results and Discussion

The welding system is shown in **Fig. 15**. Modeling of WBGFs with T-joints of 30 mm and 50 mm thickness are first used to show the effectiveness of the method proposed in this work. The weld beads during the filling stage are selected to deal with the modeling results (**Figs. 16-19**). *APWBW* measurement is conducted from top to bottom and *APWBH* measurement is carried out from left to right. The optimization process of feature point identification based on the cubic exponential smoothing method enhances the measurement accuracy of the WBGFs **(Figs. 17** and **19**).

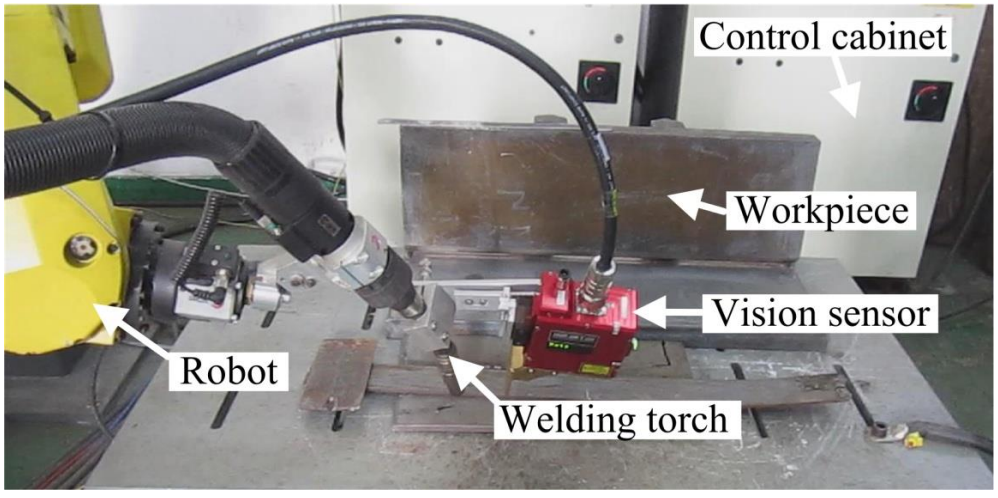


Figure 15. Welding workstation used in this study.

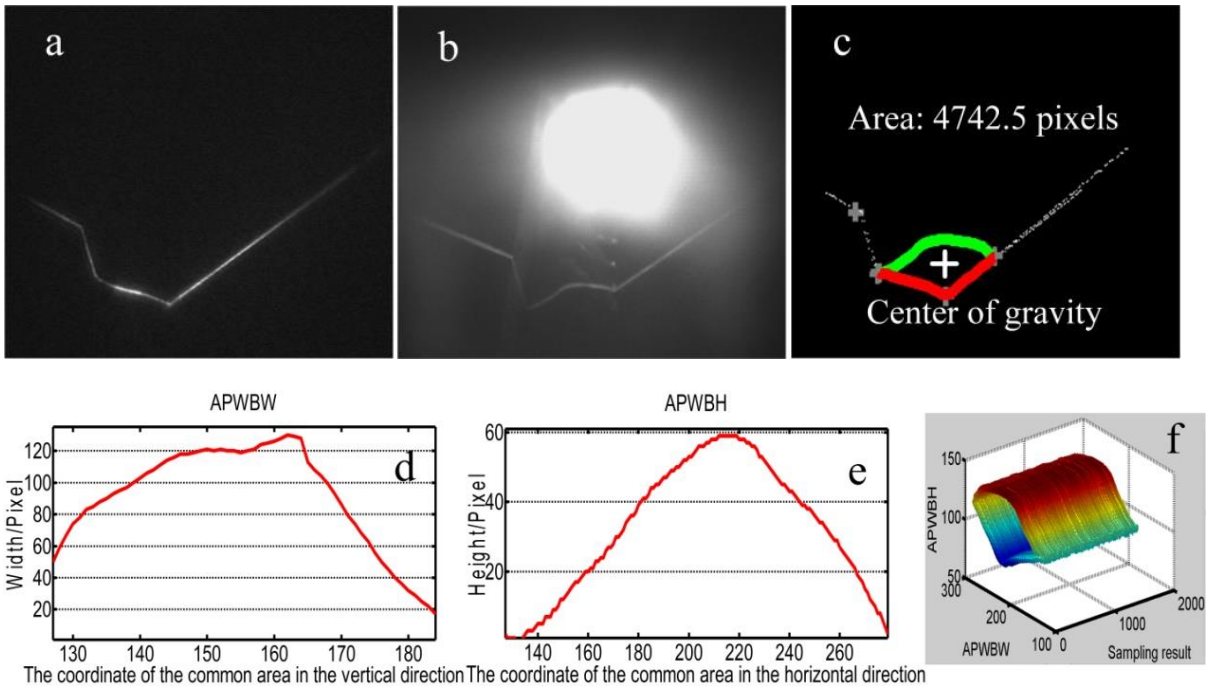


Figure 16. WBGF measurement process with a T-joint of 30 mm thickness. **a** Reference image captured before welding. **b** The current profile after a new weld bead is produced. **c** Region and area of the weld bead. **d** Measurement result of the *APWBW*. **e** Measurement result of the *APWBH*. **f** 3D reconstruction of the weld bead.

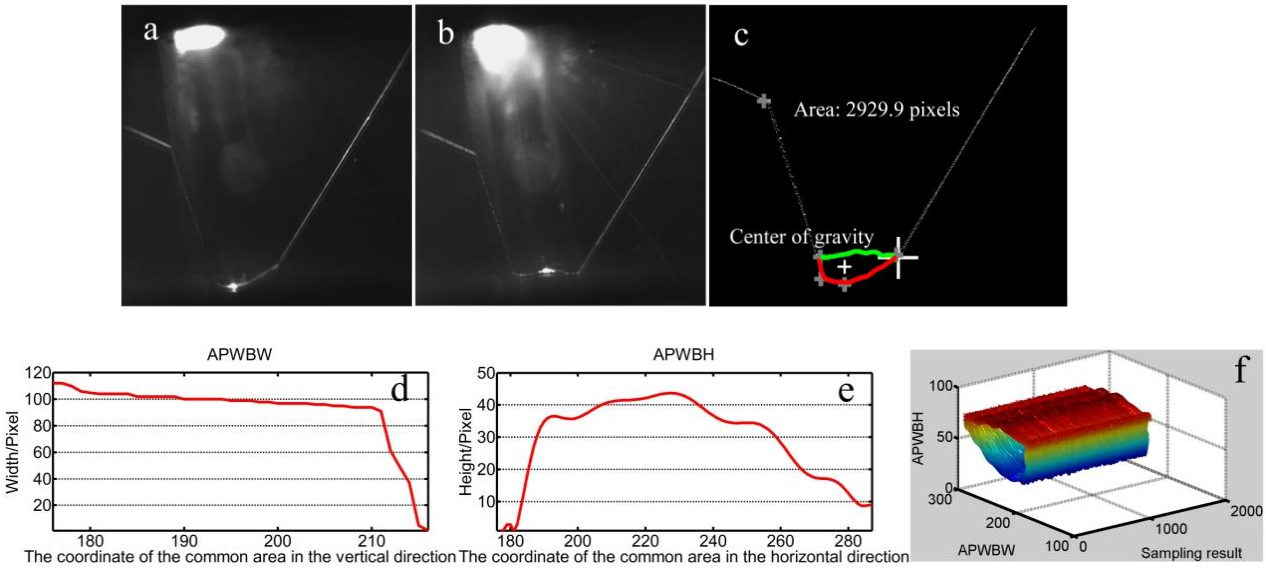


Fig. 17 WBGF measurement process with a T-joint of 50 mm thickness. **a** Reference image captured during the last welding process. **b** Current WSP. **c** Region and area of the weld bead (big white "+" represents the optimization position with the cubic exponential smoothing method). **d** Measurement result of the *APWBW*. **e** Measurement result of the *APWBH*. **f** 3D reconstruction of the weld bead.

We investigate the robustness of the measurement method proposed in this work through changing welding current to obtain the variable WSP during the same welding process. The stable measurement results show that this method can provide effective evidences to control weld

formation using the regression model between WBGFs and welding process parameters (**Figs. 18** and **19**).

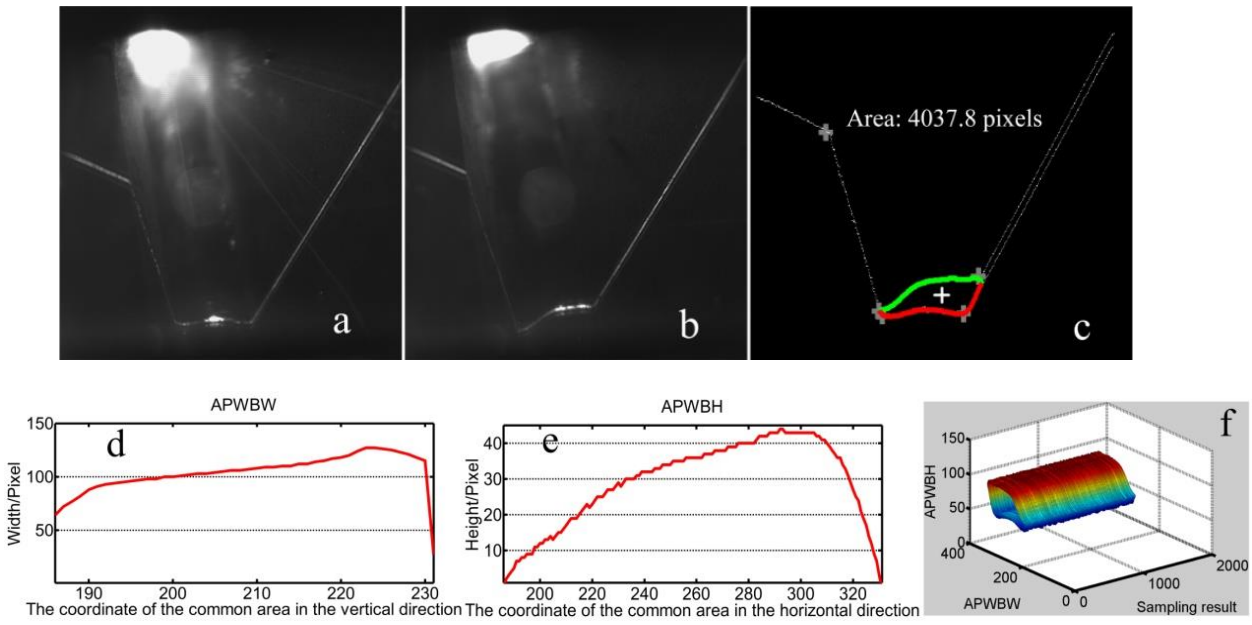


Fig. 18 Example to show that the proposed measurement method can provide effective evidences to control weld formation. **a** WSP captured during the last welding process. **b** Current WSP. **c** Region and area of the weld bead. **d** Measurement result of the *APWBW*. **e** Measurement result of the *APWBH*. **f** 3D reconstruction of the weld bead.

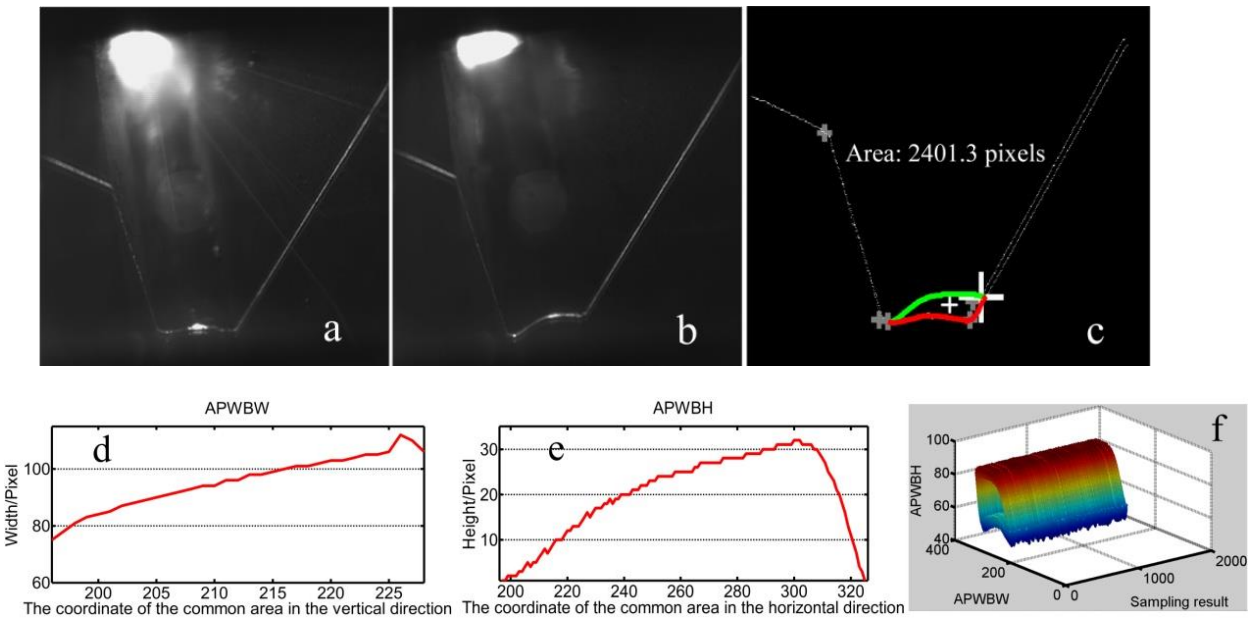


Figure 19. a WSP captured during the last welding process. **b** WSP captured during the current welding process with smaller welding current compared with **Fig. 16**. **c** Region and area of the weld bead (white "+" represents the optimization result with the cubic exponential smoothing method). **d** Measurement result of the *APWBW*. **e** Measurement result of the *APWBH*. **f** 3D reconstruction of the weld bead.

In order to further show the effectiveness of the proposed method here, two measurement processes with a butt joint of 30 mm thickness are conducted (**Figs. 20** and **21**). These experimental results show that the proposed method in this work still meets the measurement requirements of

the multipass welding process with butt joints regarding the irregular area of the bead and the *APWBW* and *APWBH*.

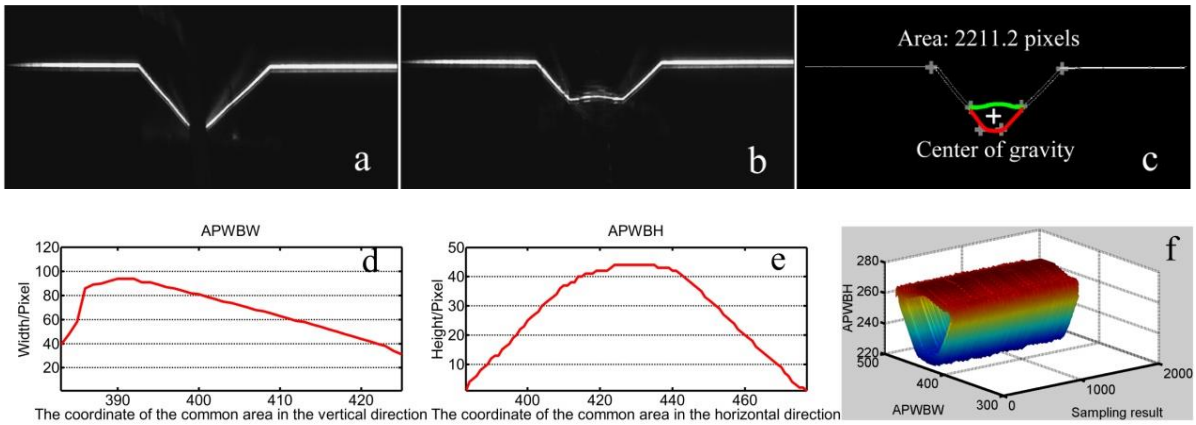


Figure 20. Example 1 using the measurement process with a butt joint to show the effectiveness of the proposed method here. **a** WSP captured before the first welding process. **b** WSP after backing welding. **c** Region and area of the weld bead. **d** and **e** are the *APWBW* and the *APWBH*, respectively. **f** 3Dreconstruction of the weld bead.

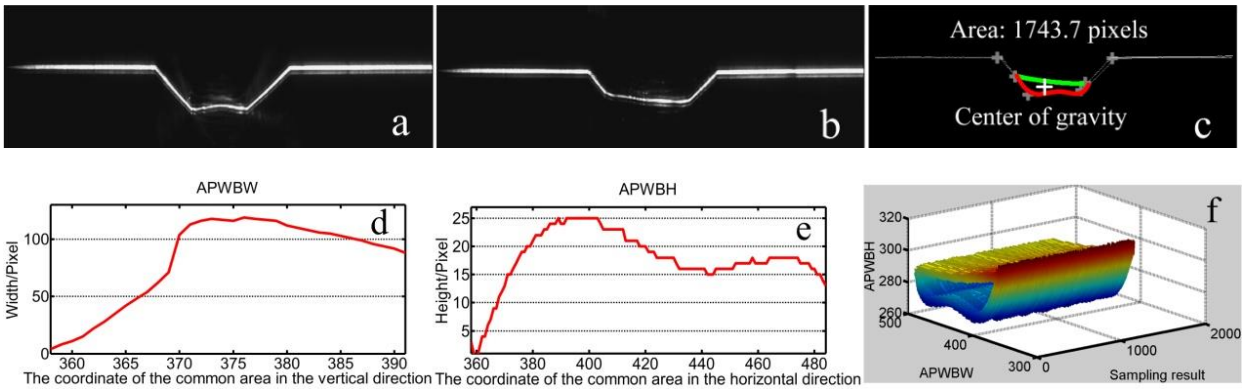


Figure 21. Example 2 using another measurement process with a butt joint to show the effectiveness of the proposed method here. **a** WSP captured before the second welding process. **b** WSP captured after the second welding process. **c** Region and area of the weld bead. **d** and **e** are the *APWBW* and the *APWBH*, respectively. **f** 3Dreconstruction of the weld bead.

We also use the modeling result on the lap-joint weld bead (**Figs. 22-24**) to show the effectiveness of the proposed method here. This method can be applied to the modeling of WBGFs with these typical joints, thin or thick steel plates.

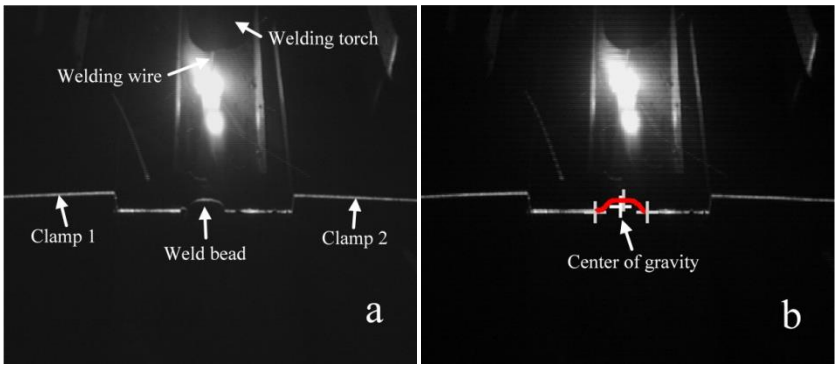


Figure 22. a Raw image with a lap joint. **b** Modeling result.

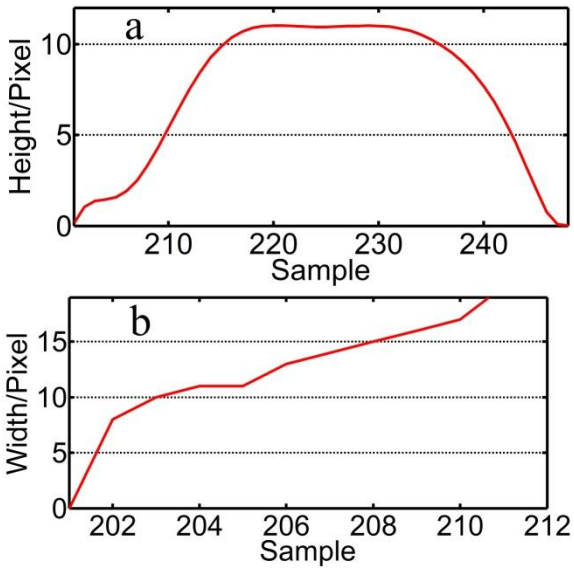


Figure 23. a All-position height and **b** width.

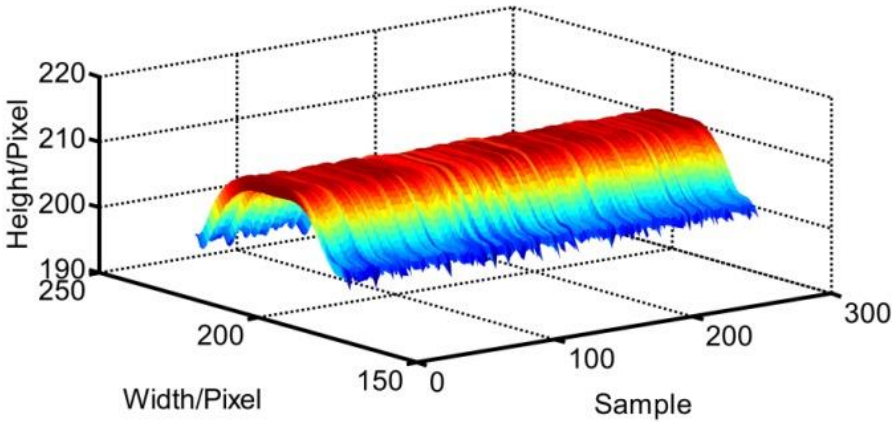


Figure 24. Three-dimensional reconstruction of the weld bead.

This paper presents an effective WBGF modeling method during the multipass GAMW process with typical joints based on machine vision and learning. This method can stably acquire the area, the center of gravity, and the *APWBW* and *APWBH* of the weld bead in real time, and expands the traditional feature measurement of irregular weld beads. It contributes on controlling weld formation and planning by providing the better evidences to optimize the welding process parameters. Also, the improvements on WBGF modeling in this work include an attempt at the real-time measurement, the investigation of the stable measurement process and the adaptability of the variable measurement objects.

The modeling experiments show that the filtering size (from 1×3 to 1×29) used to smooth the slopes is the most sensitive to the modeling results. It is necessary to develop an adaptive mechanism to approach the actual demand. This is the first aspect to be improved in the future study. Polynomial fitting is currently the popular method to model the measurement object [39]. However, there is an over-fitting phenomenon. Although this work uses piecewise fitting to respectively represent the upper and lower boundaries of the weld bead, over-fitting still happens. Another mechanism, for example, monitoring the maximum error between the last several data points of the actual boundary and the counterpart of the fitting result as a trigger to change the order of the polynomial function, should be built. The relationship between the visual features of the weld bead and welding process parameters will be investigated in the next study.

7. Conclusions

(1) The proposed visual feature extraction method adapts to the variable WSPs and provides the valuable reference to visual information acquisition for visual-sensing-based WBGF measurement.

(2) The proposed visual feature stabilization method based on the cubic exponential smoothing method shows that this optimization process increases the tracking accuracy to 1.50 pixels, which significantly increases the modeling accuracy of WBGFs.

(3) The proposed modeling method in this work can detect the area, the center of gravity and the all-position bead width and height in real time during GMAW manufacturing with typical joints, thin or thick steel plates. This modeling method provides more effective decision basis of welding process parameters to control weld formation and welding quality.

Funding acknowledge: This work is supported by the National Natural Science Foundation of China under the Grant Nos. 62066029, 51575349 and 51665037 and the Open Foundation of the Key Laboratory of Nondestructive Testing, Ministry of Education, Nanchang Hangkong University under the Grant No. EW201980090.

Reference

1. Gannon, L.; Liu, Y.; Pegg, N.; Smith, M., Effect of welding sequence on residual stress and distortion in flat-bar stiffened plates. *Mar. Struct.* **2010,** 23, (3), 385-404.
2. Wang, Z.; Zhang, Y.; Wu, L., Adaptive interval model control of weld pool surface in pulsed gas metal arc welding. *Automatica* **2012,** 48, (1), 233-238.
3. Xue, B.; Chang, B.; Peng, G.; Gao, Y.; Tian, Z.; Du, D.; Wang, G., A Vision Based Detection Method for Narrow Butt Joints and a Robotic Seam Tracking System. *Sensors* **2019,** 19, (5).
4. Zhang, Z.; Wen, G.; Chen, S., Audible Sound-based Intelligent Evaluation for Aluminum Alloy in Robotic Pulsed GTAW: mechanism, feature selection and defect detection. *IEEE T. Ind. Inform.* **2018,** 14, (7), 2973-2983.
5. Eda, S.; Ogino, Y.; Asai, S.; Hirata, Y., Numerical study of the influence of gap between plates on weld pool formation in arc spot welding process. *Weld. World* **2018,** 62, (5), 1021-1030.
6. Saravanan, S.; Sivagurumanikandan, N.; Raghukandan, K., Effect of process parameters in microstructural and mechanical properties of Nd: YAG laser welded super duplex stainless steel. *Mater. Today: Proc.* **2020**.
7. Gu, X.; KaixuanZhu; Wu, S.; Duan, Z.; Zhu, L., Effect of welding parameters on weld formation quality and tensile-shear property of laser welded SUS301L stainless steel lap filet weld. *J. Mater. Res. Technol.* **2020,** 9, (3), 4840-4854.
8. Siddaiah, A.; Singh, B. K.; Mastanaiah, P., Prediction and optimization of weld bead geometry for electron beam welding of AISI 304 stainless steel. *Int. J. Adv. Manuf. Tech.* **2017,** 89, (1), 27-43.
9. Satyanarayana, G.; Narayana, K. L.; Nageswara Rao, B., Optimal laser welding process parameters and expected weld bead profile for P92 steel. *SN Appl. Sci.* **2019,** 1, (10), 1291.
10. Sharma, P.; Mohal, S., Parametric Optimization of Submerged Arc Welding Process Parameters by Response Surface Methodology. *Mater. Today: Proc.* **2020,** 24, 673-682.
11. D.T, T.; Kim, I. s., Interaction model for predicting bead geometry for Lab Joint in GMA welding process. *Arch. Comp. Mater. Sci. & Eng.* **2009,** 1, (4), 237-244.
12. Ghosh, A.; Chattopadhyaya, S.; Hloch, S., Prediction of Weld Bead Parameters, Transient Temperature Distribution & HAZ Width of Submerged Arc Welded Structural Steel Plates. *Teh. Vjesn.* **2012,** 19, 617-620.
13. Sathiya, P.; Jaleel, M., Influence of shielding gas mixtures on bead profile and microstructural characteristics of super austenitic stainless steel weldments by laser welding. *Int. J. Adv. Manuf. Tech.* **2010,** 54, 525-535.
14. Jahanzaib, M.; Hussain, S.; Wasim, A.; Aziz, H.; Mirza, A.; Ullah, S., Modeling of weld bead geometry on HSLA steel using response surface methodology. *Int. J. Adv. Manuf. Tech.* **2017,** 89, (5), 2087-2098.

15. Neelamegam, C.; Sapineni, V.; Muthukumaran, V.; Tamanna, J., Hybrid Intelligent Modeling for Optimizing Welding Process Parameters for Reduced Activation Ferritic-Martensitic (RAFM) Steel. *J. Intell. Learn. Syst. & Appli.* **2013**, 39-47.
16. Singh, A. K.; Dey, V.; Rai, R. N.; Debnath, T., Weld Bead Geometry Dimensions Measurement based on Pixel Intensity by Image Analysis Techniques. *J. I. Eng. (India): Series C* **2019,** 100, (2), 379-384.
17. Zhang, S.; Zhang, Y.; Kovacevic, R., Noncontact Ultrasonic Sensing for Seam Tracking in Arc Welding Processes. *J. Manuf. Sci. Eng.* **1998,** 120, (3), 600-608.
18. Om, H.; Pandey, S., Effect of heat input on dilution and heat affected zone in submerged arc welding process. *Sadhana* **2013,** 38, (6), 1369-1391.
19. Xiao, R.; Xu, Y.; Hou, Z.; Chen, C.; Chen, S., An adaptive feature extraction algorithm for multiple typical seam tracking based on vision sensor in robotic arc welding. *Sensor. Actuat. A-Phys.* **2019,** 297, 111533.
20. Li, G.; Hong, Y.; Gao, J.; Hong, B.; Li, X., Welding Seam Trajectory Recognition for Automated Skip Welding Guidance of a Spatially Intermittent Welding Seam Based on Laser Vision Sensor. *Sensors* **2020,** 20, (13).
21. Xiong, J.; Zhang, G., Online measurement of bead geometry in GMAW-based additive manufacturing using passive vision. *Meas. Sci. Technol.* **2013,** 24, (11), 115103.
22. Jesús, P. L.; José, S. T. M.; Sadek, A. A., Real-Time Measurement of Width and Height of Weld Beads in GMAW Processes. *Sensors* **2016,** 16, (9), 1500.
23. Aviles-Viñas, J. F.; Rios-Cabrera, R.; Lopez-Juarez, I., On-line learning of welding bead geometry in industrial robots. *Int. J. Adv. Manuf. Tech.* **2016,** 83, (1), 217-231.
24. Rios-Cabrera, R.; Morales-Diaz, A. B.; Aviles-Viñas, J. F.; Lopez-Juarez, I., Robotic GMAW online learning: issues and experiments. *Int. J. Adv. Manuf. Tech.* **2016,** 87, (5), 2113-2134.
25. Luo, H.; Chen, X., Laser visual sensing for seam tracking in robotic arc welding of titanium alloys. *Int. J. Adv. Manuf. Tech.* **2005,** 26, (9), 1012-1017.
26. Nguyen, H.-C.; Lee, B.-R., Laser-vision-based quality inspection system for small-bead laser welding. *Int. J. Precis. Eng. Man.* **2014,** 15, (3), 415-423.
27. Chu, H.-H.; Wang, Z.-Y., A vision-based system for post-welding quality measurement and defect detection. *Int. J. Adv. Manuf. Tech.* **2016,** 86, (9), 3007-3014.
28. Yang, L.; Li, E.; Long, T.; Fan, J.; Mao, Y.; Fang, Z.; Liang, Z., A welding quality detection method for arc welding robot based on 3D reconstruction with SFS algorithm. *Int. J. Adv. Manuf. Tech.* **2018,** 94, (1), 1209-1220.
29. He, Y.; Chen, Y.; Xu, Y.; Huang, Y.; Chen, S., Autonomous Detection of Weld Seam Profiles via a Model of Saliency-Based Visual Attention for Robotic Arc Welding. *Journal of Intelligent & Robotic Systems* **2016,** 81, (3-4), 395-406.
30. He, Y.; Yu, Z.; Li, J.; Ma, G.; Xu, Y., Fault correction of algorithm implementation for intelligentized robotic multipass welding process based on finite state machines. *Robot. Comput. Integr. Manuf.* **2019,** 59, 28-35.
31. He, C.; Yan, X.; Huang, Y. In *Research on the Forecasting of Construction Accidents with the Cubic Exponential Smoothing Method*, Proceedings of the 18th International Symposium on Advancement of Construction Management and Real Estate, Berlin, Heidelberg, 2014//, 2014; Yang, D.; Qian, Y., Eds. Springer Berlin Heidelberg: Berlin, Heidelberg, 2014; pp 415-422.
32. Li, H.-A.; Zhang, M.; Yu, K.; Zhang, J.; Hua, Q.; Wu, B.; Qi, X.; Yu, Z., Combined Forecasting Model of Cloud Computing Resource Load for Energy-efficient IoT System. *IEEE Access* **2019,** 7, (99), 149542-149553.
33. He, Y.; Xu, Y.; Chen, Y.; Chen, H.; Chen, S., Weld seam profile detection and feature point extraction for multi-pass route planning based on visual attention model. *Robot. Comput. Integr. Manuf.* **2016,** 37, 251-261.
34. He, Y.; Yu, Z.; Li, J.; Yu, L.; Ma, G., Discerning Weld Seam Profiles from Strong Arc Background for the Robotic Automated Welding Process via Visual Attention Features. *Chin. J. Mech. Eng.* **2020,** 33, (1), 21.
35. Chen, H.; Liu, W.; Huang, L.; Xing, G.; Wang, M.; Sun, H., The decoupling visual feature extraction of dynamic three-dimensional V-type seam for gantry welding robot. *Int. J. Adv. Manuf. Tech.* **2015**, 1-9.
36. Lowe, D. G., Distinctive Image Features from Scale-Invariant Keypoints. *Int. J. Comput. Vision* **2004,** 60, (2), 91-110.

37. Gu, W. P.; Xiong, Z. Y.; Wan, W., Autonomous seam acquisition and tracking system for multi-pass welding based on vision sensor. *Int. J. Adv. Manuf. Tech.* **2013,** 69, (1-4), 451-460.
38. He, Y.; Yu, Z.; Li, J.; Ma, G., Weld seam profile extraction using top-down visual attention and fault detection and diagnosis via EWMA for the stable robotic welding process. *Int. J. Adv. Manuf. Tech.* **2019,** 104, (9), 3883-3897.
39. Ye, G.; Guo, J.; Sun, Z.; Li, C.; Zhong, S., Weld bead recognition using laser vision with model-based classification. *Robot. Comput. Integr. Manuf.* **2018,** 52, 9-16.